Nonlinear optical response in graphene nanoribbons: The critical role of electron scattering

F. Karimi, A. H. Davoody, and I. Knezevic

Phys. Rev. B **97**, 245403 — Published 6 June 2018

DOI: 10.1103/PhysRevB.97.245403

Nonlinear optical response in graphene nanoribbons: the critical role of electron scattering

F. Karimi,* A. H. Davoody,† and I. Knezevic‡
Department of Electrical and Computer Engineering,
University of Wisconsin-Madison, Madison, Wisconsin 53706, USA

Nonlinear nanophotonics has many potential applications, such as in mode locking, frequency-comb generation, and all-optical switching. The development of materials with large nonlinear susceptibility is key to realizing nonlinear nanophotonics. Nanostructured graphene systems, such as graphene nanoribbons and nanoislands, have been predicted to have a strong plasmon-enhanced nonlinear optical behavior in the nonretarded regime. Plasmons concentrate the light field down to subwavelength scales and can enhance the nonlinear optical effects; however, plasmon resonances are narrowband and sensitive to the nanostructure geometry. Here, we show that graphene nanoribbons, particularly armchair graphene nanoribbons, have a remarkably strong nonlinear optical response in the long-wavelength regime and over a broad frequency range, from terahertz to the nearinfrared. We use a quantum-mechanical master equation with a detailed treatment of scattering and show that, in the retarded regime, electron scattering has a critical effect on the optical nonlinearity of graphene nanoribbons, which cannot be captured *via* the commonly used relaxation-time approximation. At terahertz frequencies, where intraband optical transitions dominate, the strong nonlinearity (in particular, third-order Kerr nonlinearity) stems from the jagged shape of the electron energy distribution, caused by the interband electron scattering mechanisms along with the intraband inelastic scattering mechanisms. We show that the relaxation-time approximation fails to capture this quantum-mechanical phenomenon and results in a significant underestimation of the intraband nonlinearity. At the midinfrared to nearinfrared frequencies, where interband optical transitions dominate, the Kerr nonlinearity is significantly overestimated within the relaxation-time approximation. These findings unveil the critical effect of electron scattering on the optical nonlinearity of nanostructured graphene, and also underscore the capability of this class of materials for nonlinear nanophotonic applications.

I. INTRODUCTION

Nonlinear optics is a promising avenue for all-optical control of light [1, 2] and has many potential applications, such as in mode locking [3, 4], frequency-comb generation [5, 6], optical modulation [7–9], and all-optical switching [10]. Fulfilling the potential of nonlinear optics is conditional on the presence of strong light–matter interaction. However, nonlinear optical effects, which rely on matter-mediated photon–photon interactions, are naturally weak [11–13]. Therefore, there is ongoing research, experimental and theoretical, on finding new materials [12] and new methods[11] to enhance nonlinear optical effects.

In recent years, two-dimensional materials such as graphene, transition-metal dichalcogenides (TMDs), and phosphorene have attracted interest for nonlinear optical applications. The quantum confinement in low-dimensional materials enhances electron–light interaction and yields intriguing nonlinear optical effects. The nonlinear optical nonlinearity has been measured in graphene [14–21], TMDs [22–25], and phosphorene [26, 27], among which graphene has shown the strongest optical nonlinearity. In the telecommunication frequency window (∼1.3-1.6 μm), graphene's third-order susceptibility measured by the third-harmonic generation (THG) experiment is $\sim 10^{-15}\ \frac{\mathrm{m}^2}{\mathrm{V}^2}$ [21]. Also, there are a number of theoretical papers on the nonlinear optical properties of graphene [28–38] and nanostructured graphene, such as graphene nanoribbons (GNRs) [39, 40].

In addition to the quantum confinement in low-dimensional materials, the plasmonic field enhancement is another promising approach for amplifying nonlinear optical effects [11]. Surface plasmon polaritons, or simply plasmons, are collective oscillations of electrons in response to an external electromagnetic field [41–44]. Plasmons propagate with large wave vectors, far from the light cone (*i.e.*, in the nonretarded regime). As a result, they can concentrate the electromagnetic energy in the subwavelength limit and, consequently, can enhance the nonlinear optical response [11]. There are many papers on the plasmon-enhanced nonlinearity in graphene, graphene nanoislands, and GNRs [13, 32, 45–50]. At the near-infrared (near-IR) frequencies and for ∼10-nm-wide GNRs, the calculated plasmon-enhanced Kerr susceptibility and THG susceptibility are on the order of $10^{-12}\ \frac{\mathrm{m}^2}{\mathrm{V}^2}$ and $10^{-14}\ \frac{\mathrm{m}^2}{\mathrm{V}^2}$, respectively [45]. Although plasmons enhance the optical nonlinearity in GNRs, they make the nonlinear optical response narrowband in the frequency domain. (GNRs provide a weakly dissipative environment for plasmons, so plasmon resonances are sharp and narrow in the frequency domain).[51] Adding to this the fact that the plasmon frequencies are highly sensitive to the carrier density, nanostructure geometry,

* karimi2@wisc.edu
† davoody@wisc.edu
‡ iknezevic@wisc.edu

and edge termination, it becomes clear that a strong nonlinear material that is broadband in the retarded regime would be preferred to the plasmon enhancement approach. Such a material could be embedded in on-chip semiconductor waveguides, for the purpose of integrated nanophotonics.

Here, we show that GNRs have a remarkably strong third-order optical response in the long-wavelength regime and over a broad frequency range, from terahertz to the nearinfrared. We calculate the third-order Kerr susceptibility and the third-harmonic generation (THG) susceptibility for graphene nanoribbons (GNRs) in the long-wavelength limit. At the telecommunication frequency (∼1.3-1.6 μm), the GNRs third-order Kerr susceptibility and THG susceptibility can be as high as $\sim 10^{-10}\frac{\mathrm{m}^2}{\mathrm{V}^2}$ and $\sim 10^{-14}\frac{\mathrm{m}^2}{\mathrm{V}^2}$, respectively.

We use a perturbative approach in solving a quantum-mechanical master equation [51, 52] that accounts for electron scattering mechanisms accurately and we show that, in the retarded regime, electron scattering plays a critical role in the optical nonlinearity of GNRs, which cannot be captured with the commonly used relaxation-time approximation. At terahertz frequencies, the intraband (particularly, intrasubband) optical transitions are dominant. In this regime, the nonlinearity (in particular, the third-order Kerr nonlinearity) is strong because of the jagged shape of the electron-energy distribution, caused by the interband electron-scattering mechanisms along with the intraband inelastic electron scattering mechanisms. Only an accurate quantum-mechanical model for electron scattering is able to capture this phenomenon. In contrast, semiclassical approaches, such as the relaxation-time approximation, fail to capture the jaggedness of the electron-energy distribution and result in a significant underestimation of the intraband nonlinearity. At the midinfrared (mid-IR) to near-IR frequencies, where the interband optical transitions are dominant, the relaxation-time approximation significantly overestimates the Kerr nonlinearity. These findings underscore the critical role of electron scattering in the optical nonlinearity of nanostructured graphene, and also suggest GNRs as a suitable core material for nonlinear integrated nanophotonic applications.

II. METHODS

Here, we study the nonlinear optical response of GNRs illuminated by a TM-polarized light propagating along the ribbon (Fig. 1). We base our analysis on the self-consistent-field approximation within the Markovian master-equation formalism (SCF-MMEF), a method we developed in our previous papers [51, 52]. In the SCF-MMEF, we perturbatively solve the following master equation describing the time evolution of the density matrix in the Schrödinger picture:

$$\frac{d\rho_e(t)}{dt} = -\frac{i}{\hbar}[\mathbb{H}_{\mathrm{e}}, \rho_e(t)] - \frac{i}{\hbar}[\mathbb{V}_{\mathrm{SCF}}(t), \rho_e(t)] + \mathbb{D}\{\rho_e(t)\}. \tag{1}$$

Here, $\rho_e(t)$ is the electron density matrix, $\mathbb{H}_{\mathrm{e}}$ is the unperturbed electronic Hamiltonian, $\mathbb{V}_{\mathrm{SCF}}(t)$ is the self-consistent field, and $\mathbb{D}\{\rho_e(t)\}$ is the dissipator. The simplest form of the dissipator would be within the relaxation-time approximation (RTA), *i.e.*, $\mathbb{D}\{\rho_e(t)\} = -\frac{\rho_e(t)}{2\tau}$ (with τ being the relaxation time) [45], and we call it the RTA dissipator. The RTA assumes that all scattering mechanisms occur on the same time scales and are energy independent. However, in order to accurately account for electron scattering, we use a Lindblad-type dissipator within the Born-Markov approximation that for brevity, we call it the Lindblad dissipator [52, 55, 56]. In our calculations, we account for electron scattering *via* acoustic phonons, longitudinal optical phonons, ionized impurities, surface-optical phonons, and line-edge roughness. After solving Eq. (1) for the electron density matrix (ρ_e), we use it to calculate the macroscopic quantities such as the nonlinear conductivity, $\sigma^{(s,p_s)}$, and the nonlinear susceptibility, $\chi^{(s,p_s)}$, where s and p_s denote the response order and the corresponding harmonic, respectively. The second-order optical response vanishes because of the lattice centrosymmetry; therefore, we calculate the optical response up to third order. The third-order electron-density matrix oscillates either at the fundamental frequency (*i.e.*, Kerr nonlinearity) or at three times the fundamental frequency (*i.e.*, THG) (Fig. 1a). For the Kerr nonlinearity $(s, p_s) = (3, 1)$, and for the THG $(s, p_s) = (3, 3)$. For details of the SCF-MMEF and the Lindblad dissipator, see Appendix A.

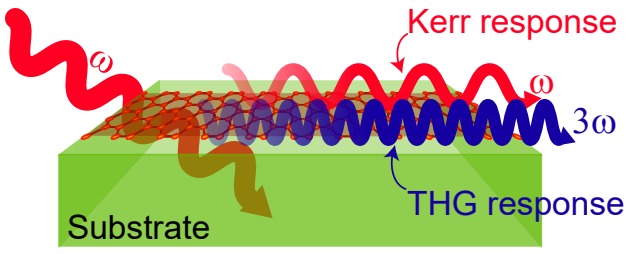

FIG. 1. Schematic of a GNR on a substrate. The incident light with frequency ω causes the third-order Kerr response (oscillating with ω) and the THG response (oscillating with 3ω).

III. RESULTS AND DISCUSSION

A. Intraband regime

At terahertz frequencies (100 GHz–10 THz) and at large-enough sheet carrier densities ($\gtrsim 10^{11}$ cm^2), the intraband (intrasubband) optical transitions dominate and the interband optical transitions are negligible. Therefore, it is appropriate to show the nonlinear optical behavior in terms of the conductivity, $\sigma^{(s,p_s)}(\omega)$. The conductivity is $\frac{\sigma_l^{(s,p_s)}}{W}$, with $\sigma_l^{(s,p_s)}$ and W being the line conductivity and the GNR width, respectively. Here, we focus on the armchair graphene nanoribbons (aGNRs), which have stronger optical nonlinearity than the zigzag graphene nanoribbons (zGNRs). The results for the nonlinear response of the zGNRs are provided in Supplemental Material [53].

aGNRs are categorized into three families, based on the number of dimers in a unit cell: $3N$, $3N+1$, and $3N+2$, with N being an integer [54]. Dimers are the carbon pairs oriented along the ribbon. $(3N+2)$-aGNRs are semimetallic and have the smallest band gap. However, by increasing the width, the band gap in all three families decreases. Calculation of the optical nonlinearity of nanomaterials requires an accurate band structure. So, we use a third-nearest-neighbor tight-binding method to calculate the band structure of hydrogen-passivated GNRs. These results are in an excellent agreement with the results of the *ab initio* calculations [54]. According to Son *et al.*, who used the local spin density approximation in their calculations, bond shortening near the edges of aGNRs, which happens because of hydrogen termination, has a crucial effect on their band structure [54]. Therefore, in our tight-binding method, we modify the edge-bond lengths, which corresponds to the change of hopping energies between carbon atoms at the edges. The details of the calculation of the aGNR band structure are provided in [51].

We begin by looking at the frequency dependence of the third-order conductivity, $\sigma^{(3)}(\omega)$. In Fig. 2, we show the magnitude of the third-order conductivity for three ∼10-nm-wide aGNRs on two different substrates: SiO_2 and hBN. The third-order conductivity asymptotically drops as ω^{-3}; however, different characteristic time scales corresponding to different electron scattering mechanisms cause deviations from the ω^{-3}-behavior. Figure 2 also shows that, between the two substrates, supported-on-hBN aGNRs show a moderately stronger nonlinearity. However, independent of the substrate or the aGNR family type, the Kerr nonlinearity is at least an order of magnitude larger than the THG. The green shaded areas in Fig. 2 illustrate the third-order conductivity calculated *via* the RTA dissipator for the relaxation times in the range of 10^{-14}–10^{-11} s. It can bee seen that, even for relaxation times as large as 10^{-11} s, the RTA dissipator significantly underestimates the third-order conductivity obtained with the accurate Lindblad-type dissipator.

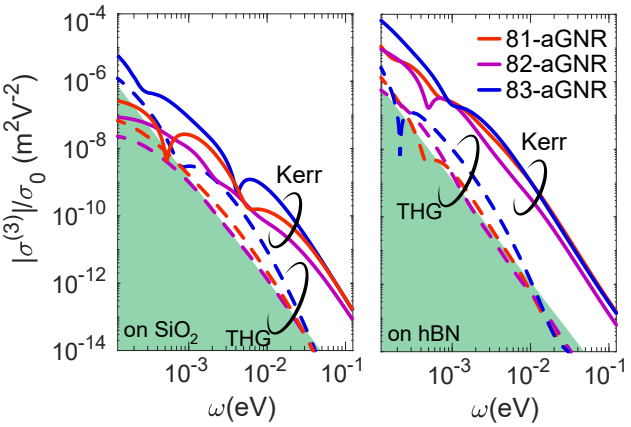

FIG. 2. The absolute value of the the third-order Kerr conductivity (solid) and the THG conductivity (dashed) for three different aGNRs, on two different substrates: SiO_2 (left) and hBN (right). The green shaded area shows the third-order conductivity calculated *via* the RTA dissipator for the relaxation times in the range of $10^{-14}-10^{-11}$ s. The sheet carrier density is 5×10^{12} cm^{-2} (*i.e.*, the line carrier density is $\sim 5\times10^6$ cm^{-1}). The third-order conductivity is normalized to $\sigma_0 = e^2/h$.

To understand the dependence of $\sigma^{(3)}(\omega)$ on the aGNR width and carrier density, we calculate the third-order conductivity for different $(3N+2)$-aGNRs at $\omega = 10$ THz ($\cong$ 41 meV) (Fig. 3). The results for zGNRs and other types of aGNRs are provided in Supplemental Material [53]. As Fig. 3 shows, the third-order nonlinearity has a strong dependence on the line carrier density and can be tuned over several orders of magnitude by changing the line carrier density or, equivalently, the Fermi level. We also calculated $\sigma^3(\omega)$ *via* the RTA dissipator with the relaxation times extracted from the *dc* mobility. The RTA dissipator (open circles in Fig. 3) not only fails to capture the carrier-density dependence, but also significantly underestimates the nonlinear conductivity in the intraband regime. To understand the reason for these behaviors, we look at the electron-energy distribution.

The perturbation expansion of the l^{th}-subband electron-energy distribution is $f_l(k) = f_l^0(k) + f_l^{(1,1)}(k) + \cdots$, where $f_l^0(k)$ is the l^{th}-subband Fermi-Dirac distribution and $f_l^{(1,1)}(k)$ is the l^{th}-subband first-order first-harmonic electron-energy distribution calculated from $\rho_e^{(1,1)}$. Figure 4 shows the first-order electron-energy distribution for the first conduction subband of a 38-aGNR, which is one of the aGNRs appearing in the valley in Fig. 3, for different carrier densities. The large third-order conductivity of GNRs occurs because the electron-energy distribution is jagged. At their onset, the inelastic intraband scattering mechanisms and the intersubband scattering mechanisms cause dips in the electron-energy distribution. The jaggedness is more pronounced near the subband extrema (owing to the large electronic

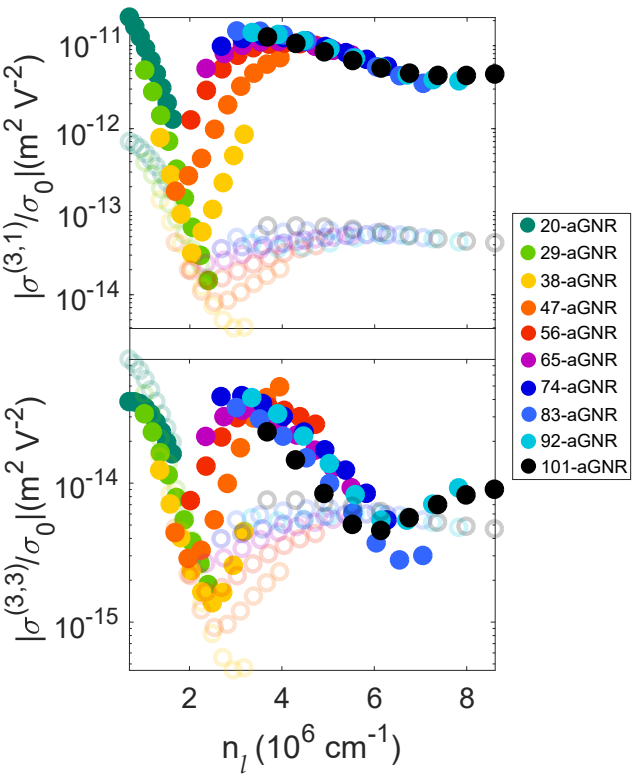

FIG. 3. The absolute value of the third-order THG conductivity (left) and the third-order Kerr conductivity (right) at 10 THz and for different $(3N+2)$-aGNRs. The third-order conductivity is calculated *via* the Lindblad dissipator (solid) and the RTA dissipator (open). The RTA dissipator significantly underestimates the third-order conductivity.

density of states) and also close to the maximum of $f_l^{(1,1)}(k)$. The $f_l^{(1,1)}(k)$ maximum occurs approximately at the Fermi energy; therefore, when the Fermi level is far from the subband extrema, the effect of electron scattering is dampened. This explains the carrier-density dependence of $\sigma^3(\omega)$ in Fig. 3. Unlike the Lindblad dissipator, the RTA dissipator fails to capture these quantum-mechanical phenomena.

In short, electron scattering plays a nontrivial role in the strong third-order optical response of GNRs at THz frequencies and requires an accurate quantum-mechanical model to be captured, rather than simplified semiclassical models based on the RTA. As a consequence of the complicated interplay among different electron-scattering mechanisms and the Fermi-level position, the third-order nonlinearity of GNRs (particularly $(3N+2)$-aGNRs) can be tuned by varying electronic density, for example by a back gate.

B. Interband regime

In the range of mid-IR to near-IR frequencies, photons have enough energy to mediate interband electronic transitions. In other words, the nonlinear optical response is dominated by the interband optical transitions instead of the intraband ones. Therefore, it is more appropriate to show the nonlinear optical response in terms of susceptibility, $\chi^{(s,p_s)}(\omega)$.

In Fig. 5, we show the third-order susceptibility, $\chi^{(3)}(\omega)$, of 81, 82, and 83-aGNRs, which are all approximately 10-nm wide. The THG susceptibility can be as large as $10^{-14}\ \frac{m^2}{V^2}$ in the near-IR and at least three orders of magnitude smaller than the third-order Kerr susceptibility. The third-order Kerr susceptibility can be as large as $10^{-10}\ \frac{m^2}{V^2}$, considerably greater than the plasmon-enhanced third-order Kerr susceptibility, which can be as large as $10^{-12}\ \frac{m^2}{V^2}$ [45]. In addition to the larger third-order susceptibility, the long-wavelength-limit nonlinear response is more broadband than the plasmon-enhanced nonlinear response. In GNRs, owing to the low electronic density of states and thus lower rates of electron scattering, plasmon resonances are sharp and narrowband [51].

In order to compare the RTA dissipator and the Lindblad dissipator, we also calculate the third-order susceptibility *via* the RTA dissipator (dashed curves in Fig. 5). We extracted the relaxation times from the *dc* mobility. The THG susceptibility calculated *via* the RTA dissipator and the Lindblad dissipator are in a good agreement with each other; however, the RTA dissipator significantly overestimates the Kerr nonlinearity, unlike in the intraband regime, in which the RTA dissipator underestimates the Kerr nonlinearity by several orders of magnitude. Moreover, the RTA dissipator does not calculate the phase of the third-order Kerr susceptibility accurately. The phase of $\chi^{(3,1)}(\omega)$ is as important as its magnitude, because it determines how the GNR $\chi^{(3,1)}(\omega)$ adds to the $\chi^{(3,1)}(\omega)$ of other materials in the waveguide. The bottom line is that the relaxation time corresponding to the *dc* mobility fails to reproduce the Kerr nonlinearity in the interband regime.

Figure 5 also shows that, in the interband regime, the third-order susceptibility has a very weak dependence on the carrier density or, equivalently, on the Fermi energy. In the interband regime, the dominant optical transitions are those happening between a full subband in the valence band and an empty subband in the conduction band; both subbands involved are far from the Fermi energy. However, this phenomenon makes the frequency dependence of the third-order susceptibility quite complex. When the frequency equals the interband oscillation energy, it is an onset of a new pathway for optical transitions and the susceptibility shows sharp jumps (Fig. 6a). This means that the third-order susceptibility strongly depends on the electron-energy dispersion, and consequently depends on the GNR edge orientation and width.

For understanding the width dependence of the GNR optical nonlinearity, we calculate the third-order Kerr susceptibility at a telecommunication frequency (1.55 μm) for different aGNRs (Fig. 6b). The aGNR widths are in the range of ∼3 to 12 nm. The Kerr susceptibility

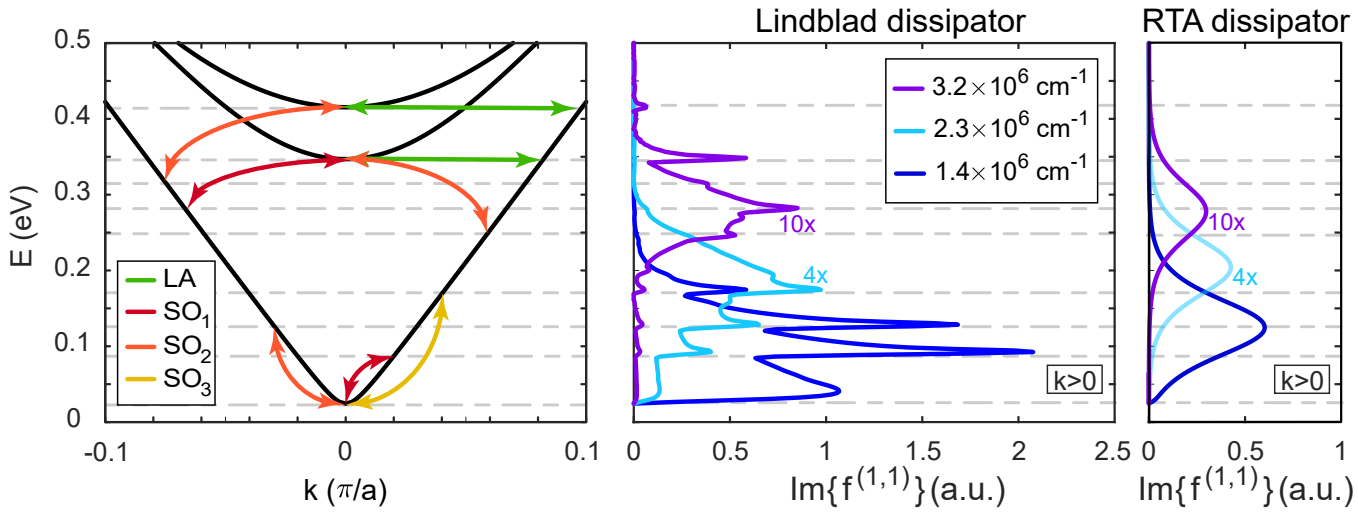

FIG. 4. (a) The electron-energy dispersion of a 38-aGNR. The arrows show a few of the electronic transitions due to different electron scattering mechanisms. (b) The first-order electron-energy distribution for the first conduction subband of the 38-aGNR for three different carrier densities. The intrasubband inelastic electron scattering mechanisms and intersubband electron-scattering mechanisms cause dips in the electron-energy distribution. For the 5×10^{12} cm^{-2} carrier density, the Fermi level is far from the subbands extrema and the electron scattering effect is reduced.

can be as large as 10^{-10} $\frac{\mathrm{m}^2}{\mathrm{V}^2}$, when an interband oscillation energy falls in the telecommunication window. This suggests that, by edge and strain engineering, one can maximize the GNRs Kerr susceptibility at the frequencies of interest. Like in the intraband regime, the hBN-supported aGNRs show a stronger optical nonlinearity than those on SiO_2. It should be noted that the Kerr nonlinear susceptibility of the zGNRs is at least an order of magnitude smaller than the Kerr nonlinear susceptibility of the aGNRs; see SM for details.

In addition to the third-order susceptibility, another important figure of merit in nonlinear-optics applications (*e.g.*, all-optical switching) is the phase shift caused by the nonlinearity, which must ideally be about π for efficient switching [12]. The phase shift, $\Delta\phi$, is equal to $\frac{E^2}{E_0^2}$, with E being the electric field. E_0 is the characteristic electric field and equals $\sqrt{\frac{|\chi^{(1,1)}|}{|\chi^{(3,1)}|}}$. The lower the characteristic electric field, the lower the electric field required to achieve the same phase change. Figure 6c shows the characteristic electric field for different aGNRs at the telecommunication frequency. The characteristic field can be as low as $\sim 5\frac{\mathrm{kV}}{\mathrm{cm}}$. Therefore, for a phase shift comparable to π, the corresponding optical field intensity can be as low as $0.3\ \frac{\mathrm{MW}}{\mathrm{cm}^2}$. Also, as a direct consequence of larger $|\chi^{(3,1)}|$ for hBN-supported aGNRs, the characteristic electric field is smaller for aGNRs supported on hBN. In short, large third-order Kerr susceptibility, along with a relatively small characteristic electric field, [12] make GNRs a promising material for nonlinear nanophotonics applications, and particularly for all-optical switching applications.

IV. CONCLUSION

In the long-wavelength regime, the third-order susceptibility (particularly the Kerr susceptibility) of GNRs (particularly, aGNRs) is remarkably large and also broadband, from terahertz to the nearinfrared. The large third-order susceptibility lowers the required optical field intensity and makes GNRs a promising material for integrated nonlinear nanophotonics applications. We used a quantum-mechanical master equation that accurately accounts for electron scattering to show that, in the retarded regime, electron scattering plays a critical role in the optical nonlinearity of GNRs. At terahertz frequencies, where the intraband optical transitions are dominant, the strong nonlinearity (in particular, third-order Kerr nonlinearity) stems from the jagged shape of the electron energy distribution, caused by the interband electron scattering mechanisms along with the intraband inelastic scattering mechanisms. The relaxation-time approximation fails to capture this quantum-mechanical phenomenon and results in a significant underestimation of the intraband nonlinearity and a significant overestimation of the interband nonlinearity. At the midinfrared and nearinfrared frequencies, the interband optical transitions are dominant and Kerr nonlinearity of GNRs can be as large as 10^{-10} $\frac{\mathrm{m}^2}{\mathrm{V}^2}$. Unlike in the intraband regime, the relaxation-time approximation significantly overestimates the Kerr nonlinearity in the interband regime. In short, electron scattering has a critical effect on the optical nonlinearity of nanostructured graphene and must be accurately computed within a quantum transport framework.

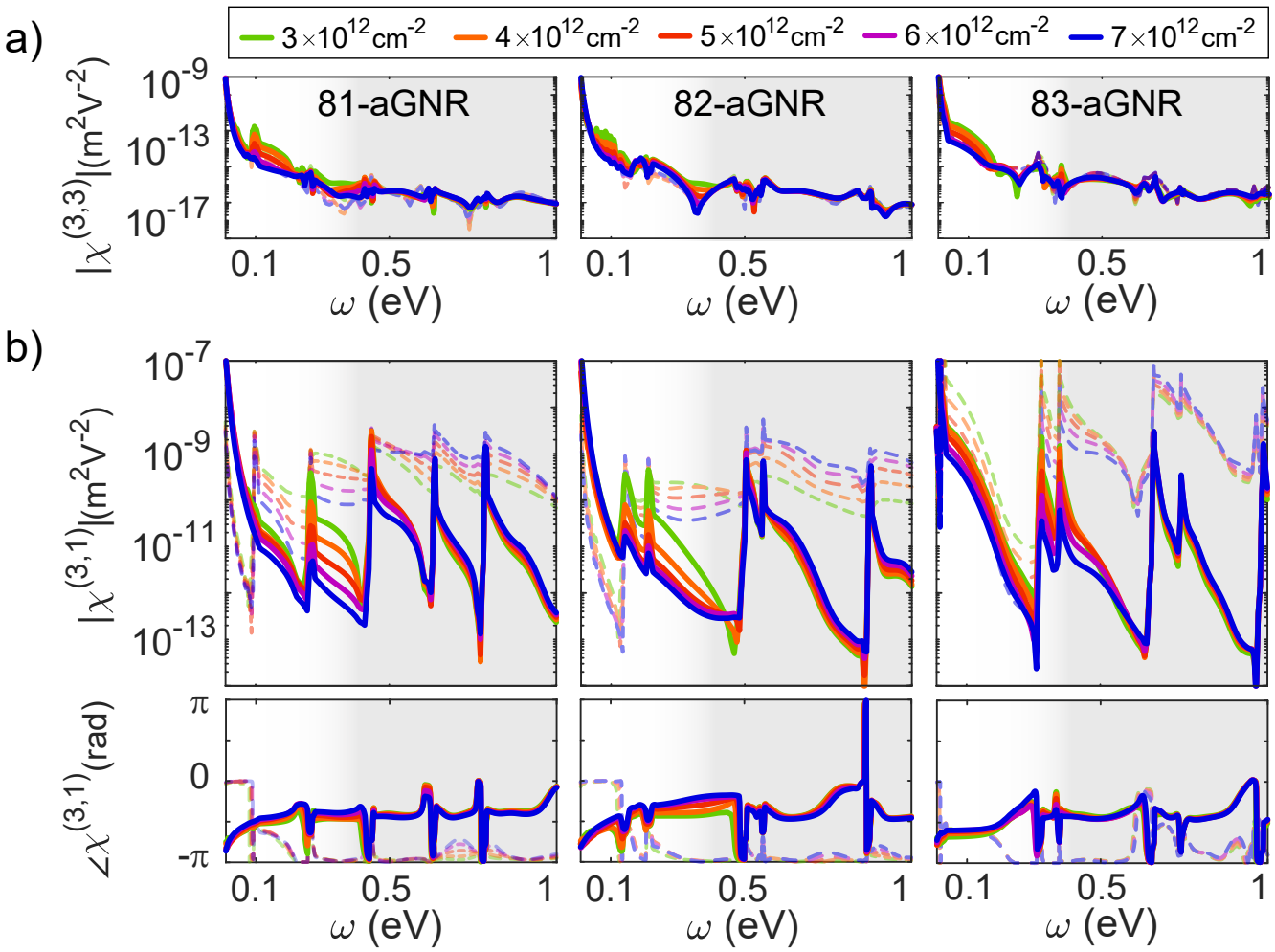

FIG. 5. a) The magnitude of the THG susceptibility. The Lindblad-dissipator results (solid) and RTA-dissipator results (dashed) are very close to each other. b) The magnitude (top row) and the phase (bottom row) of the third-order Kerr susceptibility. The RTA dissipator significantly overestimates the third-order Kerr susceptibility magnitude and also does not calculate the phase accurately. The dark background shade in the panels denotes the near-IR region.

ACKNOWLEDGMENTS

The authors gratefully acknowledge support by the U.S. Department of Energy, Office of Basic Energy Sciences, Division of Materials Sciences and Engineering, Physical Behavior of Materials Program, under Award DE-SC0008712. This work was performed using the compute resources and assistance of the UW-Madison Center for High Throughput Computing (CHTC) in the Department of Computer Sciences.

Appendix A: Nonliear response via SCF-MMEF

Here, we use the SCF-MMEF along with the perturbation theory to calculate the nonlinear optical response of GNRs. The self-consistent potential energy, with the frequency of ω and the wave vector of q, can be written as $V_{\rm SCF}(t) = V_{\rm SCF}e^{iqx-i\omega t} + V^*_{\rm SCF}e^{-iqx+i\omega t}$, where x-axis is aligned along the GNR. By assuming the self-consistent field as the perturbation, the s^{th}-order p_s^{th}-harmonic conductivity, we start with the continuity equation, $-e\omega n_\ell^{(s,p_s)} = qJ_\ell^{(s,p_s)}$, where n_ℓ and J_ℓ are, respectively, the induced charge line density and the induced current line density and are assumed to be uniformly distributed across the ribbon. (Note: ℓ denotes line.) Also, the constitutive relation between the self-consistent electric field and the current density is $J_\ell^{(s,p_s)} = \sigma_\ell^{(s,p_s)}(E_{\rm SCF})^{p_s+\frac{s-p_s}{2}}(E^*_{\rm SCF})^{\frac{s-p_s}{2}}$, with σ_ℓ being the line conductivity. Incorporating the continuity equation, the constitutive equation, and $-eE_{\rm SCF} = -iqV_{\rm SCF}$, we obtain

$$\sigma_\ell^{(s,p_s)}(q,\omega) = \frac{(-i)^{p_s}e\omega}{q^2}\left(\frac{e}{q}\right)^{s-1}P_\ell^{(s,p_s)}(q,\omega). \qquad \text{(A1)}$$

In the above equation, $P_\ell^{(s,p_s)}$ is the line polarization and is defined as the ratio between the induced charge line

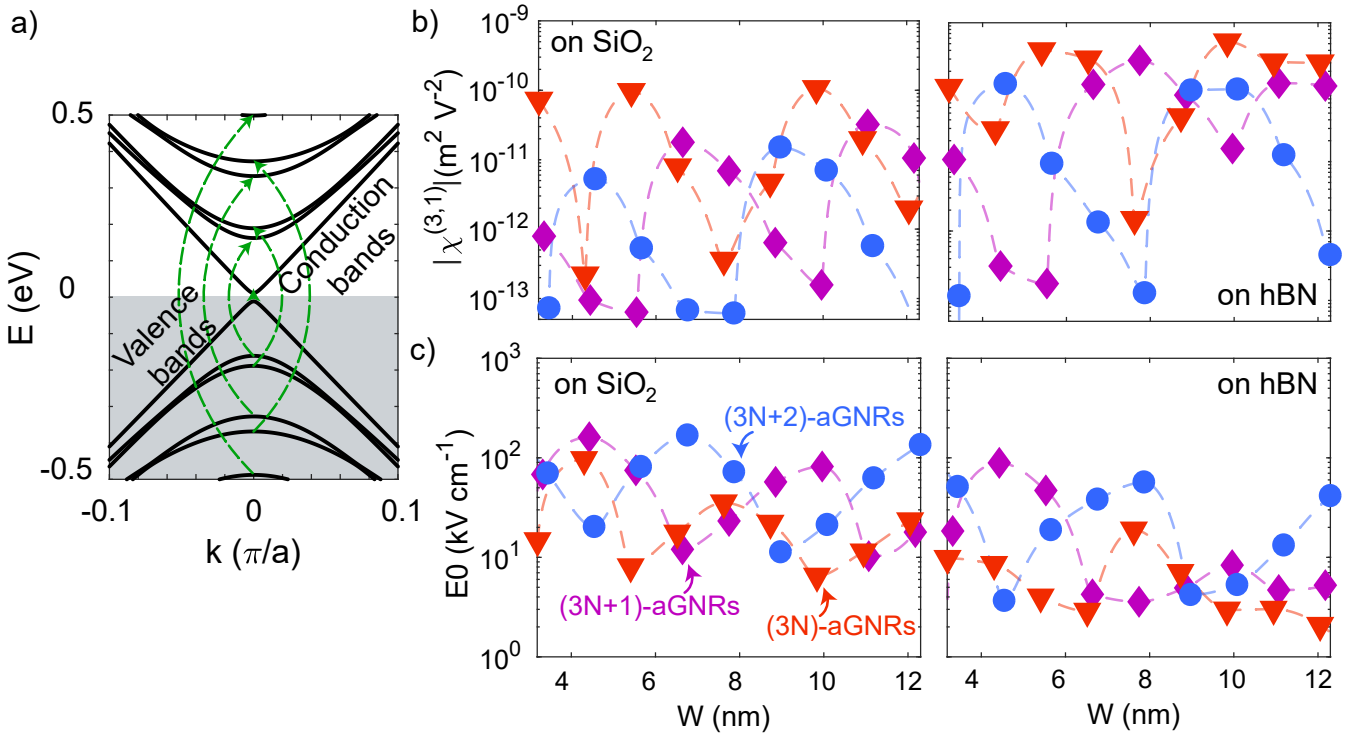

FIG. 6. (a) The electron energy dispersion of a 83-aGNR. The arrows show interband optical transitions. (b) The third-order Kerr susceptibility at the telecommunication frequency for different $(3N)$-aGNRs (triangle), $(3N+1)$-aGNRs (diamond), and $(3N+2)$-aGNRs (circle). The aGNRs are supported on SiO_2 (left) and hBN (right). We calculated the third-order Kerr susceptibility *via* the Lindblad dissipator. (c) The characteristic electric field at the telecommunication frequency for different aGNRs on SiO_2 (left) and hBN (right).

density and the self-consistent field:

$$P_\ell^{(s,p_s)}(q,\omega) = \frac{-en_l^{(s,p_s)}(q,\omega)}{{V_{\rm SCF}}^{p_s+\frac{s-p_s}{2}}{V^*_{\rm SCF}}^{\frac{s-p_s}{2}}}. \tag{A2}$$

The s^{th}-order line polarization defined above has units of $\frac{\rm C}{\rm m\ J^s}$. To avoid confusion, we denote the (volume) polarization (the dipole moment volume density) with $\mathcal{P}$. The (volume) polarization $\mathcal{P}$ and the induced charge volume density relate as $iq\mathcal{P}^{(s,p_s)} = -\frac{en_\ell^{(s,p_s)}}{Wd}$, where W and d are the width and the thickness of the GNR, respectively. Incorporating this equation, the constitutive equation $\mathcal{P}^{(s,p_s)} = \epsilon_0\chi^{(s,p_s)}(E_{\rm SCF})^{p_s+\frac{s-p_s}{2}}(E^*_{\rm SCF})^{\frac{s-p_s}{2}}$, and Eq. (A1) yields

$$\chi^{(s,p_s)}(q,\omega) = \frac{i\sigma^{(s,p_s)}}{\epsilon_0 p_s\omega d}, \tag{A3}$$

where $\chi^{(s,p_s)}$ is the nonlinear susceptibility and $\sigma = \frac{\sigma_\ell}{W}$ denotes the nonlinear (sheet) conductivity. Knowing the nonlinear conductivity [Eq. (A1)] and, consequently, the nonlinear susceptibility [Eq. (A3)] requires knowing the polarization, $P_\ell^{(s,p_s)}$. We generalize the SCF-MMEF [51, 52] to calculate the nonlinear polarization. We start with the total Hamiltonian within the self-consistent-field approximation that is $\mathbb{H}(t) = \mathbb{H}_{\rm e} + \mathbb{V}_{\rm SCF}(t) + \mathbb{H}_{\rm col} + \mathbb{H}_{\rm ph}$. $\mathbb{H}_{\rm e}$ is the unperturbed Hamiltonian of the electronic system, with the eigenkets and eigenenergies of $\mathbb{H}_{\rm e}$ being represented by $|kl\rangle$ and ϵ_{kl}, respectively. k is the wave vector along the x axis, l is the band index. (Note: l denotes the subband index and ℓ denotes line.) $\mathbb{H}_{\rm ph}$ denotes the free Hamiltonian of the phonon bath. Also, $\mathbb{H}_{\rm col}$ corresponds to the collision Hamiltonian. All interaction Hamiltonian can be written in the following general form $\mathbb{H}_{\rm int} = \sum_{kq,l'l}\mathcal{M}_{\rm int}(q)(k+ql'|kl)c^\dagger_{k+ql'}c_{kl}\otimes\mathbb{B}_{q,v}$, where c and $c^\dagger$ are the electron annihilation and creation operators, respectively. $\mathcal{M}_{\rm int}(q)$ is the interaction strength. $\mathbb{B}_{q,v}$ operates on the phonon bath and $(k+ql'|kl)$ is the overlap integrals. The details of the interaction Hamiltonian and also, the self-consistent field calculation are provided in [51]. The polarization in the second-quantization representation reads

$$P_\ell^{(s,p_s)}(q,\omega) = -\frac{e}{L}\sum_{k,l',l}\frac{\langle c^\dagger_{kl}c_{k+p_sql'}\rangle^{(s,p_s)}}{{V_{\rm SCF}}^{p_s+\frac{s-p_s}{2}}{V^*_{\rm SCF}}^{\frac{s-p_s}{2}}} \times (kl|k+p_sql'), \tag{A4}$$

where $\langle c^\dagger_{kl}c_{k+p_sql'}\rangle = {\rm tr_e}\{c^\dagger_{kl}c_{k+p_sql'}\rho_e\}$, is the expectation value of the coherences. Now, we calculate the time dependence of the expected value of the coherences *via*

a quantum master equation. Within the *Born approximation* and *Markov approximation* [51, 52, 55, 56], the equation of motion of the electron-density matrix is

$$\frac{d\rho_e(t)}{dt} = -\frac{i}{\hbar}[\mathbb{H}_{\rm e}, \rho_e(t)] - \frac{i}{\hbar}[\mathbb{V}_{\rm SCF}(t), \rho_e(t)] - \frac{1}{\hbar^2}\int_0^\infty d\tau\ {\rm tr}_{\rm ph}\left\{[\mathbb{H}_{\rm col}, [\tilde{\mathbb{H}}_{\rm col}(-\tau), \rho_e(t)\otimes\rho_{\rm ph}]]\right\}. \tag{A5}$$

The tilde symbol denotes the operators in the interaction picture, *i.e.* $\tilde{\mathbb{O}}(t) = \mathbb{U}_0^\dagger(t)\mathbb{O}(t)\mathbb{U}_0(t)$. $\mathbb{U}_0$ is the unitary time-evolution operator corresponding to $\mathbb{H}_{\rm e} + \mathbb{V}_{\rm SCF}(t) + \mathbb{H}_{\rm ph}$. Now, We use a perturbative approach to solve Eq. (A5) for the density operator. The perturbation expansion of the electron-density matrix is $\rho_e(t) = \sum_s \rho_e^{(s)}(t) = \sum_{s,p_s} \rho_e^{(s,p_s)} e^{-ip_s\omega t} + {\rm h.c.}$ By substituting the perturbation expansion of the density matrix into Eq. (A5), solving it for the time harmonic solutions, knowing that $\mathbb{V}_{\rm SCF}(t)$ has no diagonal elemnts, and keeping only the s^{th}-order and p_s^{th}-harmonic terms, we get

$$-i\omega\rho_e^{(s,p_s)} = -\frac{i}{\hbar}[\mathbb{H}_{\rm e}, \rho_e^{(s,p_s)}] - \frac{i}{\hbar}[\mathbb{V}_{\rm SCF}, \rho_e^{(s-1,p_s\pm1)}] - \frac{1}{\hbar^2}\int_0^\infty d\tau\ {\rm tr}_{\rm ph}\left\{[\mathbb{H}_{\rm col}, [e^{-\frac{i}{\hbar}(\mathbb{H}_e+\mathbb{H}_{ph})\tau}\mathbb{H}_{\rm col}e^{\frac{i}{\hbar}(\mathbb{H}_e+\mathbb{H}_{ph})\tau}, \rho_e^{(s,p_s)}\otimes\rho_{\rm ph}]]\right\}. \tag{A6}$$

Now, by following the same procedure as in Ref. [52], we use the above equation to obtain the equation of motion for $\langle c_{kl}^\dagger c_{k+p_sql'}\rangle^{(s,p_s)}$:

$$\begin{aligned}
\hbar p_s\omega\langle c_{kl}^\dagger c_{k+p_sql'}\rangle^{(s,p_s)} &= (\epsilon_{k+p_sql'} - \epsilon_{kl})\langle c_{kl}^\dagger c_{k+p_sql'}\rangle^{(s,p_s)} \\
&+ V_{\rm SCF}\sum_{k'mm'} {\rm tr}_e\left\{\left[c_{k'+qm'}^\dagger c_{k'm}, \rho_e^{(s-1,p_s-1)}\right] c_{kl}^\dagger c_{k+p_sql'}\right\}(k'+qm'|k'm) \\
&+ V_{\rm SCF}^*\sum_{k'mm'} {\rm tr}_e\left\{\left[c_{k'-qm'}^\dagger c_{k'm}, \rho_e^{(s-1,p_s+1)}\right] c_{kl}^\dagger c_{k+p_sql'}\right\}(k'-qm'|k'm) \\
&+ i\pi\sum_{k'mm'g}\Big[\delta(\epsilon_{k'm} - \epsilon_{kl} \pm \hbar\omega_g)\left(\mathcal{W}_{k'-k,g}^{\pm} \pm \Delta\mathcal{W}_{k'-k,g}f_{kl}\right) \\
&\qquad\times(k+p_sql'|k'+p_sqm')(k'm|kl)\langle c_{k'm}^\dagger c_{k'+p_sqm'}\rangle^{(s,p_s)}\Big] \\
&+ i\pi\sum_{k'mm'g}\Big[\delta(\epsilon_{k'+p_sqm'} - \epsilon_{k+p_sql'} \pm \hbar\omega_g)\left(\mathcal{W}_{k'-k,g}^{\pm} \pm \Delta\mathcal{W}_{k'-k,g}f_{k+p_sql'}\right) \\
&\qquad\times(k'm|kl)(k+p_sql'|k'+p_sqm')\langle c_{k'm}^\dagger c_{k'+p_sqm'}\rangle^{(s,p_s)}\Big] \\
&- i\pi\sum_{k'mm'g}\Big[\delta(\epsilon_{k'm'} - \epsilon_{km} \pm \hbar\omega_g)\left(\mathcal{W}_{k'-k,g}^{\mp} \mp \Delta\mathcal{W}_{k'-k,g}f_{k'm'}\right) \\
&\qquad\times(k'm'|kl)(km|k'm')\langle c_{km}^\dagger c_{k+p_sql'}\rangle^{(s,p_s)}\Big] \\
&- i\pi\sum_{k'mm'g}\Big[\delta(\epsilon_{k'+p_sqm} - \epsilon_{k+p_sqm'} \pm \hbar\omega_g)\left(\mathcal{W}_{k'-k,g}^{\mp} \mp \Delta\mathcal{W}_{k'-k,g}f_{k'+p_sqm}\right) \\
&\qquad\times(k+p_sql'|k'+p_sqm)(k'+p_sqm|k+p_sqm')\langle c_{kl}^\dagger c_{k+p_sqm'}\rangle^{(s,p_s)}\Big].
\end{aligned} \tag{A7}$$

$\mathcal{W}_{k'-k,v}^{\pm}$ is the scattering weight. The expression for the scattering weights of the acoustic-phonon scattering, longitudinal-optical scattering, ionized-impurity scattering, line-edge-roughness scattering, and the surface-optical-phonon (SO-phonon) scattering is provided in Ref. [51].

Phonon–phonon scattering results in a finite phonon lifetime [57, 58]. This, of course, holds for SO phonons in polar materials, such as SiO_2 or hBN, as well. The finite lifetime of SO phonons is equivalent to their broadened energy ($\hbar\Delta\omega_{\rm SO}$), which can be seen in their transmittance spectra obtained via spectrometry. We extract the broadening of the SO-phonon energies in SiO_2 and hBN from their complex dielectric function [52]. We consider the full width at half maximum (FWHM) of the imaginary part of the dielectric function at a SO-phonon

resonance as its energy broadening. The broadening energy of SO-phonons in SiO_2 and hBN is approximately 4-6 meV, which is not negligible and its effect on the electron-SO-phonon scattering needs to be taken into account. To do so, we substitute a SO-phonon mode at ω_{SO} with the corresponding scattering weight of $\mathcal{W}$ with three SO-phonon modes at $\omega_{SO} - \frac{\Delta\omega_{SO}}{2}$, ω_{SO}, and $\omega_{SO} + \frac{\Delta\omega_{SO}}{2}$ with the corresponding scattering weights of $\frac{1}{4}\mathcal{W}$, $\frac{1}{2}\mathcal{W}$, and $\frac{1}{4}\mathcal{W}$, respectively.

Depending on the nature of optical transitions in different regimes of interest, Eq. (A7) can be simplified, considerably. In the intraband regime, we could assume that for $l \neq l'$, $\langle c^\dagger_{kl} c_{k+p_s ql}\rangle^{(s,p_s)} = 0$. In the interband and the long-wavelength regime, the optical transitions between the corresponding valence and conduction subbands are dominant. As a result, Eq. (A7) can be decoupled into pairs of l^{th}-conduction and l^{th}-valence subbands. In order to solve Eq. (A7) numerically, we discretize the Brillouin zone and rewrite Eq. (A7) in the matrix form:

$$\begin{aligned}\mathcal{E}^{(s,p_s)}\mathcal{X}^{(s,p_s)} =& \mathcal{F}^{(s,p_s)} \\ &+ i(\mathcal{R}^{(s,p_s)} - \mathcal{R}'^{(s,p_s)} - \mathcal{R}''^{(s,p_s)})\mathcal{X}^{(s,p_s)},\end{aligned} \tag{A8}$$

where

$$\mathcal{E}^{(s,p_s)}_{\{kl'l\}\{k'm'm\}} = \delta_{\{kl'l\}\{k'm'm\}}(\epsilon_{kl} - \epsilon_{k+p_s ql'} + \hbar\omega), \tag{A9aa}$$

$$\mathcal{X}^{(s,p_s)}_{\{kl'l\}} = \frac{\langle c^\dagger_{kl} c_{k+p_s ql'}\rangle^{(s,p_s)}}{{V_{\text{SCF}}}^{p_s+\frac{s-p_s}{2}} V^*_{\text{SCF}}{}^{\frac{s-p_s}{2}}}, \tag{A9ab}$$

$$\begin{aligned}\mathcal{R}^{(s,p_s)}_{\{kl'l\}\{k'm'm\}} =& \frac{L}{\hbar}\sum_{\substack{g \\ \epsilon_{k'+p_s qm'} = \epsilon_{k+p_s ql'} \mp \hbar\omega_g}} \frac{\left[\mathcal{W}^{\pm}_{k'-k,g} \pm \Delta\mathcal{W}_{k'-k,g} f_{k+p_s ql'}\right]}{\left|\frac{\partial\epsilon_{k'+p_s qm}}{\partial k'}\right|}(k'm|kl)(k+p_s ql'|k'+p_s qm') \\ &+ \frac{L}{\hbar}\sum_{\substack{g \\ \epsilon_{k'm} = \epsilon_{kl} \mp \hbar\omega_g}} \frac{\left[\mathcal{W}^{\pm}_{k'-k,g} \pm \Delta\mathcal{W}_{k'-k,g} f_{kl}\right]}{\left|\frac{\partial\epsilon_{k'm}}{\partial k'}\right|}(k+p_s ql'|k'+p_s qm')(k'm|kl),\end{aligned} \tag{A9ac}$$

$$\mathcal{R}'^{(s,p_s)}_{\{kl'l\}\{kl'm\}} = \frac{L}{\hbar}\sum_{\substack{m'g \\ \epsilon_{k'm'} = \epsilon_{km} \mp \hbar\omega_g}} \frac{\left[\mathcal{W}^{\mp}_{k'-k,g} \mp \Delta\mathcal{W}_{k'-k,g} f_{k'm'}\right]}{\left|\frac{\partial\epsilon_{k'm}}{\partial k'}\right|}(k'm'|kl)(km|k'm'), \tag{A9ad}$$

$$\begin{aligned}\mathcal{R}''^{(s,p_s)}_{\{kl'l\}\{km'l\}} =& \frac{L}{\hbar}\sum_{\substack{mg \\ \epsilon_{k'+p_s qm} = \epsilon_{k+p_s qm'} \mp \hbar\omega_g}} \frac{\left[\mathcal{W}^{\mp}_{k'-k,g} \mp \Delta\mathcal{W}_{k'-k,g} f_{k'+p_s qm}\right]}{\left|\frac{\partial\epsilon_{k'+p_s qm}}{\partial k'}\right|} \\ &\times (k+p_s ql'|k'+p_s qm)(k'+p_s qm|k+p_s qm')\,.\end{aligned} \tag{A9ae}$$

And for $s > 1$,

$$\begin{aligned}\mathcal{F}^{(s,p_s)}_{\{kl'l\}} =& \sum_{k'm}\frac{\langle c^\dagger_{kl} c_{k+(p_s-1)qm}\rangle^{(s-1,p_s-1)}}{{V_{\text{SCF}}}^{p_s+\frac{s-p_s}{2}-1} V^*_{\text{SCF}}{}^{\frac{s-p_s}{2}}}(k+p_s ql'|k+(p_s-1)qm) \\ &- \sum_{k'm}\frac{\langle c^\dagger_{k+qm} c_{k+p_s ql'}\rangle^{(s-1,p_s-1)}}{{V_{\text{SCF}}}^{p_s+\frac{s-p_s}{2}-1} V^*_{\text{SCF}}{}^{\frac{s-p_s}{2}}}(k+qm|kl) \\ &+ \sum_{k'm}\frac{\langle c^\dagger_{kl} c_{k+(p_s+1)qm}\rangle^{(s-1,p_s+1)}}{{V_{\text{SCF}}}^{p_s+\frac{s-p_s}{2}} V^*_{\text{SCF}}{}^{\frac{s-p_s}{2}-1}}(k+p_s ql'|k+(p_s+1)qm) \\ &- \sum_{k'm}\frac{\langle c^\dagger_{k-qm} c_{k+p_s ql'}\rangle^{(s-1,p_s+1)}}{{V_{\text{SCF}}}^{p_s+\frac{s-p_s}{2}} V^*_{\text{SCF}}{}^{\frac{s-p_s}{2}-1}}(k-qm|kl).\end{aligned} \tag{A9b}$$

It should be noted that $\langle c^\dagger_{kl} c_{k-p_s ql'}\rangle^{(s,-p_s)} = \left[\langle c^\dagger_{k-p_s ql'} c_{kl}\rangle^{(s,p_s)}\right]^*$. For $s = 1$, $\mathcal{F}^{(1,1)}_{\{kl'l\}} =$

$(f_{kl} - f_{k+ql'})(k + ql'|kl)$. By solving Eq. (A8) for $\mathcal{X}^{(s,p_s)}$, we use equation Eq. (A4) to calculate the polarization, and consequently, the nonlinear conductivity and the nonlinear susceptibility.

[1] R. W. Boyd, *Nonlinear Optics, Third Edition* (Academic Press, 2008), 3rd ed., ISBN 0123694701, 9780123694706.
[2] E. Garmire, Optics Express **21**, 30532 (2013).
[3] E. P. Ippen, Applied Physics B **58**, 159 (1994), ISSN 1432-0649, URL `https://doi.org/10.1007/BF01081309`.
[4] R. Paschotta and U. Keller, Applied Physics B **73**, 653 (2001), ISSN 1432-0649, URL `https://doi.org/10.1007/s003400100726`.
[5] P. DelHaye, A. Schliesser, O. Arcizet, T. Wilken, R. Holzwarth, and T. Kippenberg, Nature **450**, 1214 (2007).
[6] T. Sakamoto, T. Kawanishi, and M. Izutsu, Optics Letters **32**, 1515 (2007).
[7] M. Liu, X. Yin, E. Ulin-Avila, B. Geng, T. Zentgraf, L. Ju, F. Wang, and X. Zhang, Nature **474**, 64 (2011).
[8] G. T. Reed, G. Mashanovich, F. Gardes, and D. Thomson, Nature Photonics **4**, 518 (2010).
[9] Z. Sun, A. Martinez, and F. Wang, Nature Photonics **10**, 227 (2016).
[10] C. Koos, P. Vorreau, T. Vallaitis, P. Dumon, W. Bogaerts, R. Baets, B. Esembeson, I. Biaggio, T. Michinobu, F. Diederich, et al., Nature Photonics **3**, 216 (2009).
[11] M. Kauranen and A. V. Zayats, Nature Photonics **6**, 737 (2012).
[12] J. Khurgin, Applied Physics Letters **104**, 161116 (2014).
[13] F. J. Garcia de Abajo and J. D. Cox, Nature Communications **5** (2014).
[14] E. Hendry, P. J. Hale, J. Moger, A. Savchenko, and S. Mikhailov, Physical review Letters **105**, 097401 (2010).
[15] T. Gu, N. Petrone, J. F. McMillan, A. van der Zande, M. Yu, G.-Q. Lo, D.-L. Kwong, J. Hone, and C. W. Wong, Nature Photonics **6**, 554 (2012).
[16] R. Wu, Y. Zhang, S. Yan, F. Bian, W. Wang, X. Bai, X. Lu, J. Zhao, and E. Wang, Nano Letters **11**, 5159 (2011).
[17] H. Zhang, S. Virally, Q. Bao, L. K. Ping, S. Massar, N. Godbout, and P. Kockaert, Optics Letters **37**, 1856 (2012).
[18] N. Kumar, J. Kumar, C. Gerstenkorn, R. Wang, H.-Y. Chiu, A. L. Smirl, and H. Zhao, Physical Review B **87**, 121406 (2013).
[19] S.-Y. Hong, J. I. Dadap, N. Petrone, P.-C. Yeh, J. Hone, and R. M. Osgood Jr, Physical Review X **3**, 021014 (2013).
[20] N. Vermeulen, D. Castelló-Lurbe, J. Cheng, I. Pasternak, A. Krajewska, T. Ciuk, W. Strupinski, H. Thienpont, and J. Van Erps, Physical Review Applied **6**, 044006 (2016).
[21] A. Saynatjoki, L. Karvonen, J. Riikonen, W. Kim, S. Mehravar, R. A. Norwood, N. Peyghambarian, H. Lipsanen, and K. Kieu, ACS Nano **7**, 8441 (2013).
[22] D. Li, W. Xiong, L. Jiang, Z. Xiao, H. Rabiee Golgir, M. Wang, X. Huang, Y. Zhou, Z. Lin, J. Song, et al., ACS Nano **10**, 3766 (2016).
[23] R. Woodward, R. Murray, C. Phelan, R. de Oliveira, T. Runcorn, E. Kelleher, S. Li, E. de Oliveira, G. Fechine, G. Eda, et al., 2D Materials **4**, 011006 (2016).
[24] R. Wang, H.-C. Chien, J. Kumar, N. Kumar, H.-Y. Chiu, and H. Zhao, ACS Applied Materials & Interfaces **6**, 314 (2013).
[25] A. Säynätjoki, L. Karvonen, H. Rostami, A. Autere, S. Mehravar, A. Lombardo, R. A. Norwood, T. Hasan, N. Peyghambarian, H. Lipsanen, et al., Nature Communications **8** (2016).
[26] N. Youngblood, R. Peng, A. Nemilentsau, T. Low, and M. Li, ACS Photonics **4**, 8 (2017), http://dx.doi.org/10.1021/acsphotonics.6b00639, URL `http://dx.doi.org/10.1021/acsphotonics.6b00639`.
[27] H.-Y. Wu, Y. Yen, and C.-H. Liu, Applied Physics Letters **109**, 261902 (2016).
[28] S. Mikhailov, EPL (Europhysics Letters) **79**, 27002 (2007).
[29] S. A. Mikhailov, Physical Review B **93**, 085403 (2016).
[30] A. Marini, J. Cox, and F. G. de Abajo, Physical Review B **95**, 125408 (2017).
[31] H. Rostami and M. Polini, Physical Review B **93**, 161411 (2016).
[32] H. Rostami, M. I. Katsnelson, and M. Polini, Physical Review B **95**, 035416 (2017).
[33] J. Cheng, N. Vermeulen, and J. Sipe, New Journal of Physics **16**, 053014 (2014).
[34] J. L. Cheng, N. Vermeulen, and J. Sipe, Physical Review B **91**, 235320 (2015).
[35] Y. Wang, M. Tokman, and A. Belyanin, Physical Review B **94**, 195442 (2016).
[36] T. Christensen, W. Yan, A.-P. Jauho, M. Wubs, and N. A. Mortensen, Physical Review B **92**, 121407 (2015).
[37] V. A. Margulis, E. Muryumin, and E. Gaiduk, Solid State Communications **246**, 76 (2016).
[38] V. A. Margulis, E. Muryumin, and E. Gaiduk, Journal of Optics **19**, 065505 (2017).
[39] Y. Wang and D. R. Andersen, Journal of Physics D: Applied Physics **49**, 46LT01 (2016).
[40] Y. Wang and D. R. Andersen, Journal of Physics: Condensed Matter **28**, 475301 (2016).
[41] J. A. Schuller, E. S. Barnard, W. Cai, Y. C. Jun, J. S. White, and M. L. Brongersma, Nature Materials **9**, 193 (2010).
[42] S. A. Maier, M. L. Brongersma, P. G. Kik, S. Meltzer, A. A. Requicha, and H. A. Atwater, Advanced Materials **13**, 1501 (2001).
[43] S. A. Maier and H. A. Atwater, Journal of Applied Physics **98**, 10 (2005).
[44] A. Karalis, E. Lidorikis, M. Ibanescu, J. Joannopoulos, and M. Soljačić, Physical Review Letters **95**, 063901 (2005).
[45] J. D. Cox, I. Silveiro, and F. J. Garca de Abajo, ACS Nano **10**, 1995 (2016), pMID: 26718484, http://dx.doi.org/10.1021/acsnano.5b06110, URL `http:`

//dx.doi.org/10.1021/acsnano.5b06110.
[46] J. D. Cox and F. J. Garca de Abajo, ACS Photonics **2**, 306 (2015), http://dx.doi.org/10.1021/ph500424a, URL http://dx.doi.org/10.1021/ph500424a.
[47] J. D. Cox, A. Marini, and F. J. G. De Abajo, Nature Communications **8** (2017).
[48] M. Gullans, D. Chang, F. Koppens, F. G. de Abajo, and M. D. Lukin, Physical Review Letters **111**, 247401 (2013).
[49] X. Yao, M. Tokman, and A. Belyanin, Physical Review Letters **112**, 055501 (2014).
[50] A. Gorbach, Physical Review A **87**, 013830 (2013).
[51] F. Karimi and I. Knezevic, Physical Review B **96**, 125417 (2017).
[52] F. Karimi, A. Davoody, and I. Knezevic, Physical Review B **93**, 205421 (2016).
[53] See Supplemental Material at [URL] for additional details and results, which includes Refs. [51,54] .
[54] Y.-W. Son, M. L. Cohen, and S. G. Louie, Physical Review Letters **97**, 216803 (2006).
[55] H.-P. Breuer and F. Petruccione, *The theory of open quantum systems* (Oxford University Press on Demand, 2002).
[56] I. Knezevic and B. Novakovic, Journal of Computational Electronics **12**, 363 (2013).
[57] J. M. Ziman, *Electrons and phonons: the theory of transport phenomena in solids* (Oxford university press, 1960).
[58] G. P. Srivastava, *The physics of phonons* (CRC press, 1990).